

Fracture mechanics of brick masonry: size effects and snap-back analysis

PIETRO BOCCA

Istituto Universitario di Architettura di Venezia, 30125 Venezia, Italy

ALBERTO CARPINTERI, SILVIO VALENTE

Politecnico di Torino, Dipartimento di Ingegneria Strutturale, Corso Duca degli Abruzzi 24, 10129 Torino, Italy

Fracture energy, G_F , and the critical value of stress-intensity factor, K_{IC} , are determined for brick masonry specimens tested in bending with different notch depths. The experimental results are compared with numerical simulations, obtained through a cohesive crack model developed originally for concrete. Theoretical and experimental load-deflection curves present very similar softening branches. In some cases, a snap-back instability is predicted by the model and confirmed by the experimental data. A size-scale transition appears evident from an ultimate strength collapse at the ligament to a brittle fracture due to stress-intensification. Such a transition demonstrates that LEFM is a very suitable model for brick masonry structures at the usual size-scale. A non-dimensional brittleness number is introduced as a measure of the LEFM applicability.

NOTATION

a	Crack length
E	Young's modulus
f_t	Ultimate tensile strength
G_F	Fracture energy
K_{IC}	Stress-intensity factor (critical value)
l	Support span
L, H, B	Length, depth, thickness of the specimen
P	Load
δ	Loading point displacement
ν	Poisson ratio
W_O	Area under the $P-\delta$ curve
σ	Stress acting on the crack surfaces
w	Crack opening displacement
w_c	Critical value of the crack opening displacement
w	Vector of the crack opening displacements
$[k]$	Matrix of the coefficients of influence (nodal forces)
F	Vector of the nodal forces
c	Vector of the coefficients of influence (external load)
Γ	Vector of the crack opening displacements due to the specimen weight

1. INTRODUCTION

Brick masonry failures have been extensively investigated through uniaxial and biaxial loading conditions [1–3], and the cracking evolution, from microcracking to macrofracture, can be analysed by means of recently established experimental techniques. On the other

hand, when the dissipative phenomena play an important role, as, for example, in the case of masonry structures in seismic zones, energy criteria analyse the failure mechanism better and more realistically than the classical stress criteria. The application of fracture mechanics, whose concepts are already used for steel and concrete successfully [4, 5], is extended herein to brick masonry. It is demonstrated how the theoretical results fit with the experimental ones satisfactorily. Further investigations are encouraged with the following objects:

- (i) to characterize the different brick masonry materials;
- (ii) to simulate numerically the mechanical and failure behaviour of brick masonry structures even of complex geometrical shape.

The problem of the Mode I (opening) fracture mechanism in brick masonry is faced. Structural elements working in compression often undergo this mode of failure [6]. The fracture energy G_F and the critical value K_{IC} of stress-intensity factor [4] are evaluated for three-point bending specimens, directly drilled from historical bricks. Such experimental data, obtained for different materials and different notch depths, are then put in comparison with numerical results derived from a cohesive crack finite-element simulation, originally developed for concrete [4]. Theoretical and experimental load-deflection curves present very similar softening branches. In some cases, a snap-back instability is predicted by the model and confirmed by the experimental investigation. A softening branch with positive slope is revealed experimentally by controlling the crack mouth

opening displacement, and numerically by controlling the crack length. Both such quantities are thus monotonically increasing with time. Otherwise, when the controlling parameter is the beam deflection, unstable and catastrophic behaviour occurs with a brittle fracture.

An evident transition appears from an ultimate strength collapse at the ligament, to a brittle crack propagation due to stress-intensification, by increasing the dimensionless size Hf_t/G_F . In the present paper, the brittleness number variation is produced by varying the material properties f_t , G_F , and not the size scale H , as done in previous studies [7].

2. SPECIMEN PREPARATION AND EXPERIMENTAL PROCEDURE

The specimens' features (Fig. 1) are listed in Table 1. The capital letters A, B, C refer to three different structures, built respectively in the 19th (A, B) and 20th (C) century.

Three-point bending tests according to the RILEM recommendation for concrete [8] were carried out, through an MTS machine with maximum load up to 20 kN. Load-deflection ($P-\delta$) diagrams were plotted by controlling the crack mouth opening displacement. The latter was increased at a constant rate of $2.5 \times 10^{-7} \text{ m s}^{-1}$ (Fig. 2).

3. COHESIVE CRACK MODEL

The cohesive crack model, developed originally for concrete, is based on the following assumptions [4, 5]:

1. The cohesive fracture zone (plastic or process zone) begins to develop when the maximum principal stress achieves the ultimate tensile strength f_t (Fig. 3a).
2. The material in the process zone is partially damaged but still able to transfer stress. Such a stress is dependent on the crack opening displacement w . A linear $\sigma-w$ law is assumed as in Fig. 3b.

The real crack tip is defined as the point where the distance between the crack surfaces is equal to the

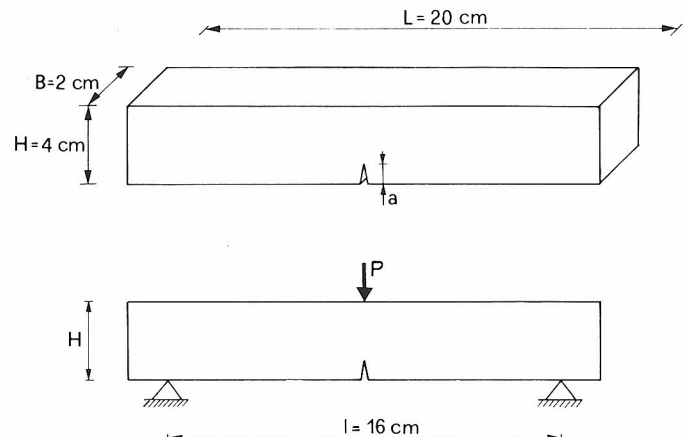


Fig. 1 Geometry of the masonry specimens and three-point bending scheme.

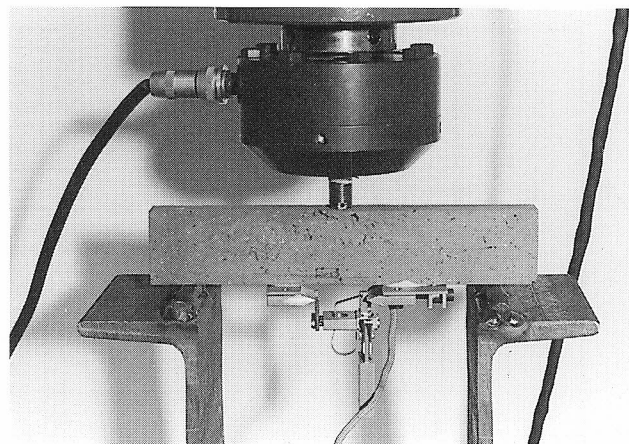


Fig. 2 Testing apparatus and crack mouth opening control system.

critical value of crack opening displacement w_c and the normal stress vanishes (Fig. 4a). On the other hand, the fictitious crack tip is defined as the point where the normal stress attains the maximum value f_t and the crack opening vanishes (Fig. 4a).

Table 1 Specimen details

Specimen	Size (10^{-2} m)			Notch depth (10^{-2} m)	Notch thickness (10^{-2} m)	Density (kg m^{-3})	Young's modulus (MPa)	Tensile strength (MPa)
	L	H	B					
A1	20	4	2.0	0.4	0.100	0.1	1718	1900
A2	20	4	2.2	1.1	0.275			2.2
A3	20	4	2.0	1.9	0.475			
B1	20	4	1.9	0.4	0.100	0.1	1750	1880
B2	20	4	1.9	1.1	0.275			1.5
B3	20	4	2.3	1.9	0.475			
C1	20	4	1.9	0.4	0.100	0.1	1809	4900
C2	20	4	2.0	1.1	0.275			10.0
C3	20	4	2.0	1.9	0.475			

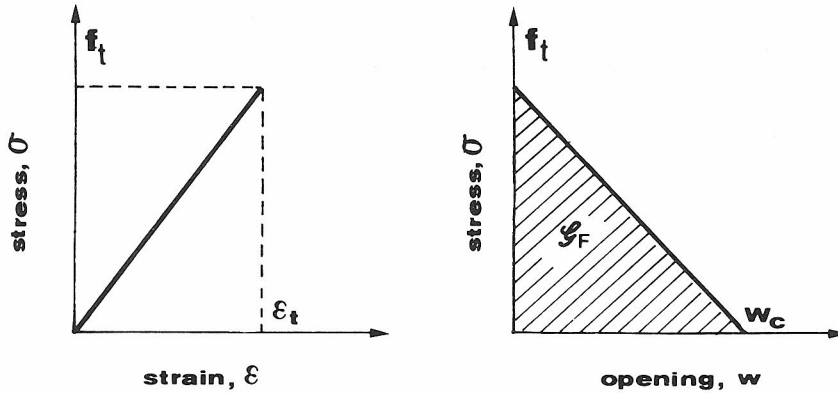


Fig. 3(a) Stress-strain law of the material outside the damage zone and (b) stress-crack opening displacement law of the damage zone.

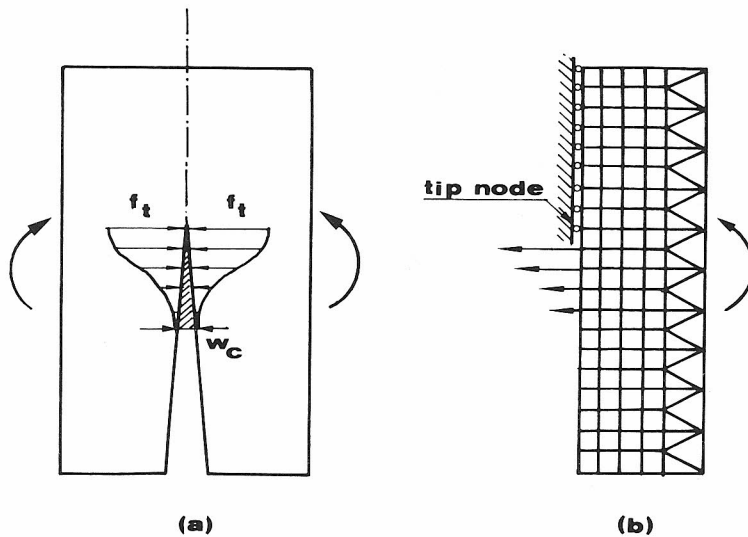


Fig. 4(a) Stress acting across the cohesive crack and (b) equivalent nodal forces in the finite-element mesh.

The closing stresses acting on the crack surfaces (Fig. 4a) can be replaced by nodal forces (Fig. 4b). The intensity of these forces depends on the opening of the fictitious crack, w , according to the σ - w constitutive law of the material (Fig. 3b). When the tensile strength f_t is achieved at the fictitious crack tip (Fig. 4b), the top node is opened and a cohesive force starts acting across the crack, while the fictitious crack tip moves to the next node.

With reference to the three-point bending test (TPBT) geometry in Fig. 5, the nodes are distributed along the potential fracture line. The coefficients of influence in terms of node openings and deflection are computed by a finite-element analysis where the fictitious structure in Fig. 5 is subjected to $(n+1)$ different loading conditions. Consider the TPBT in Fig. 6a with the initial crack tip in the node k . The crack opening displacement at the n fracture nodes may be expressed as follows:

$$\mathbf{w} = [k] \mathbf{F} + \mathbf{c} P + \mathbf{l} \quad (1)$$

On the other hand, the initial crack is stress-free and therefore

$$F_i = 0 \quad i = 1, \dots, (k-1) \quad (2a)$$

while at the ligament there is no displacement discontinuity:

$$w_i = 0 \quad i = k, (k+1), \dots, n \quad (2b)$$

Equations 1 and 2 constitute a linear algebraic systems of $2n$ equations in $2n$ unknowns, i.e. the elements of vectors \mathbf{w} and \mathbf{F} . If load P and vector \mathbf{F} are known, it is possible to compute the beam deflection, δ :

$$\delta = \mathbf{C}^T \mathbf{F} + D_p P + D_\gamma \quad (3)$$

where D_p is the deflection for $P = 1$ and D_γ is the deflection due to the specimen weight.

After the first step, a cohesive zone forms in front of the real crack tip (Fig. 6b), say between nodes j and l .

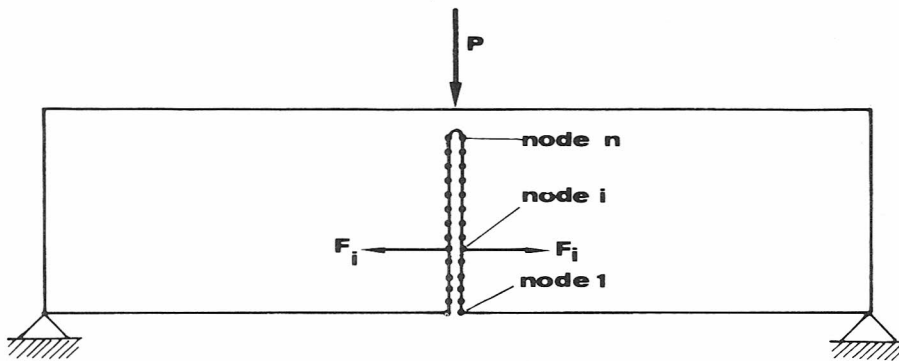


Fig. 5 Finite-element nodes along the potential crack line.

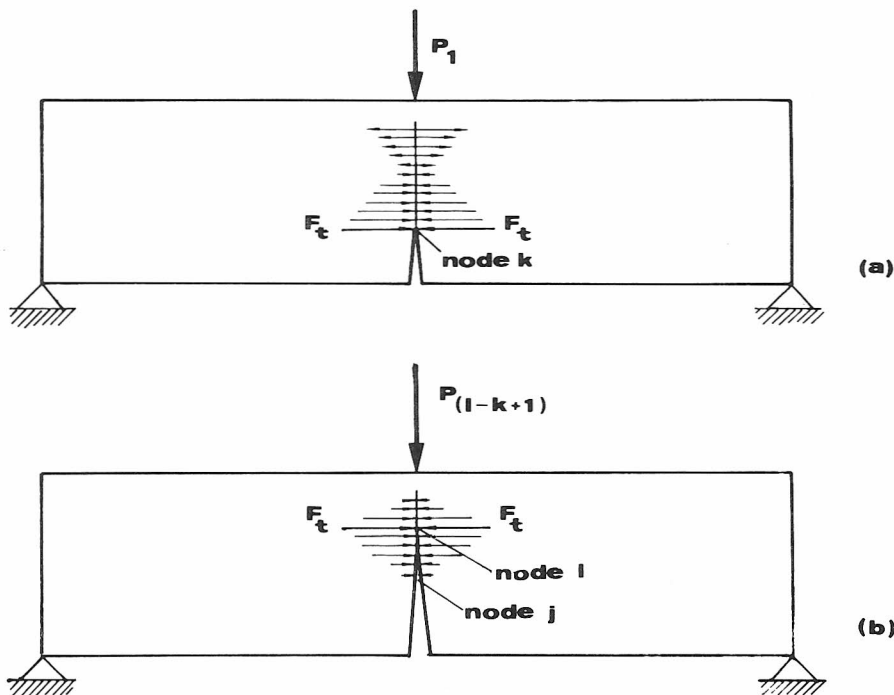


Fig. 6 Cohesive crack at (a) the first loading step and (b) the $(l - k + 1)$ th loading step.

Then Equations 2 are replaced by

$$F_i = 0 \quad i = 1, 2, \dots, (j-1) \quad (4a)$$

$$F_i = F_t(1 - w_i/w_c) \quad i = j, (j+1), \dots, 1 \quad (4b)$$

$$w_i = 0 \quad i = 1, \dots, n \quad (4c)$$

where F_t is the ultimate-strength nodal force:

$$F_t = f_t H/(n+1) \quad (5)$$

Equations 1 and 4 constitute a linear algebraical system of $(2n+1)$ equations and $(2n+1)$ unknowns, i.e. the elements of vectors \mathbf{w} and \mathbf{F} and the external load \mathbf{P} .

At the first step, the cohesive zone is missing ($l = j = k$) and the load P_1 producing the ultimate-strength nodal force F_t at the initial crack tip (node k) is computed. Such a value P_1 , together with the related

deflection δ_1 computed through Equation 3, gives the first point of the $P-\delta$ curve. At the second step, the cohesive zone is between the nodes k and $(k+1)$, and the load P_2 producing the force F_t at the second fictitious crack tip (node $k+1$) is computed. Equation 3 then provides the deflection δ_2 . At the third step, the fictitious crack tip is in the node $(k+2)$, and so on. The present numerical program simulates a loading process where the controlling parameter is the fictitious crack depth. On the other hand the real (stress-free) crack depth, external load and deflection are obtained at each step after an iterative procedure.

The program stops with the untying of node n and, consequently, with the determination of the last couple of values F_n and δ_n . In this way, the complete load-deflection curve is automatically plotted by the computer.

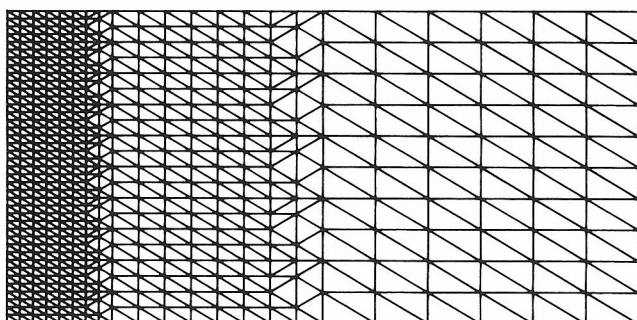


Fig. 7 Finite-element mesh ($n = 39$).

In the case under consideration, the finite-element simulation was realized with the mesh sketched in Fig. 7 ($n = 39$), using constant-strain triangles.

4. DISCUSSION

The fracture energy G_F is obtained from the load-deflection curves (Figs 8 to 10), taking into account the area under the curve divided by the ligament area. The G_F values are reported in Table 2. It is worth noting that they are varying with the material and turn out to be almost independent of notch depth. Such values are of the same order of magnitude as those of standard concretes [9].

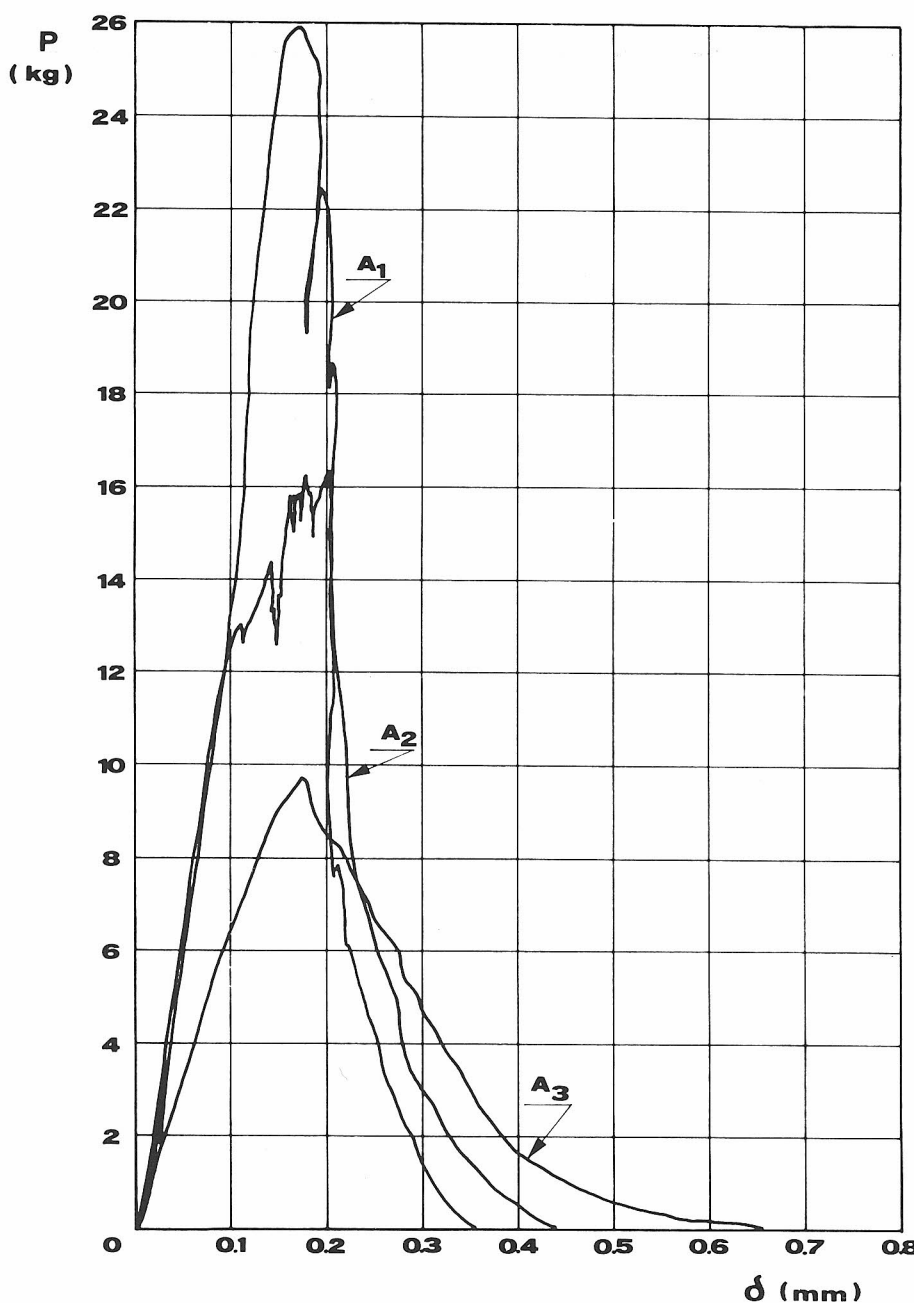


Fig. 8 Load-deflection diagrams obtained experimentally on masonry of the 19th century (material A).

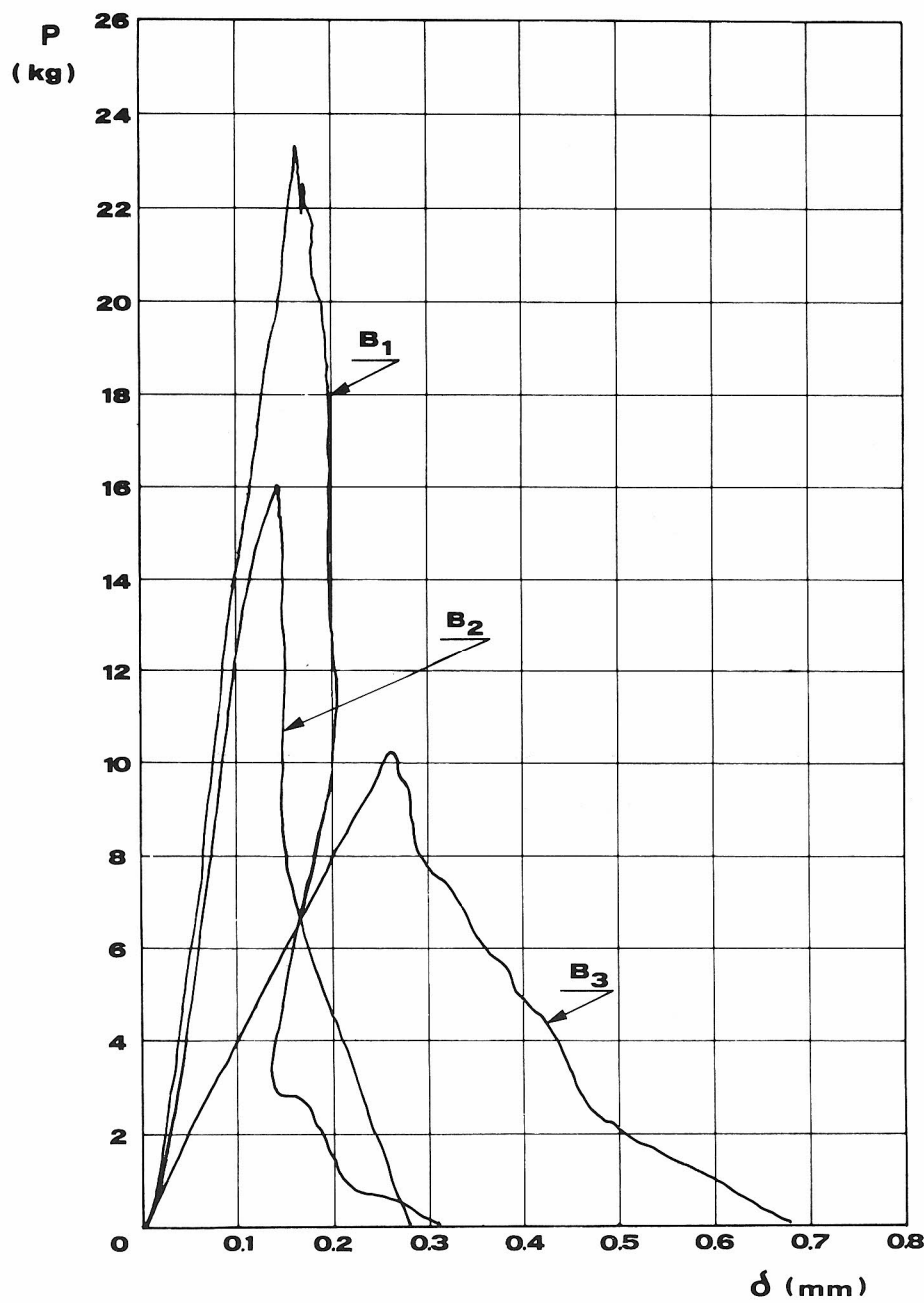


Fig. 9 Load-deflection diagrams obtained experimentally on masonry of the 19th century (material B).

The critical value of stress-intensity factor is derived from the following well-known relation [9]:

$$K_{IC} = (G_F E)^{1/2} \quad (6)$$

The K_{IC} values, listed in Table 2, are slightly lower than those relating to concrete, due to the smaller Young's modulus of bricks.

In Figs 8 to 10 it is shown how the softening branch varies with the initial notch depth in the brick specimen. Specimens with shallow notches behave brittler than those with deeper notches.

The numerical simulation, performed with the cohe-

Table 2 Experimental results

Specimen	G_F (N m ⁻¹)	G_F mean value (N m ⁻¹)	K_{IC} (kN m ^{-3/2})	K_{IC} mean value (kN m ^{-3/2})
A1	52.40	52.20	315.5	313.9
A2	41.30		280.1	
A3	63.10		346.2	
B1	33.80	37.20	252.0	263.7
B2	32.40		246.8	
B3	45.50		292.4	
C1	59.50	52.10	540.0	505.0
C2	50.20		496.0	
C3	46.70		478.0	
Portland		10 to 100		500 to 2000

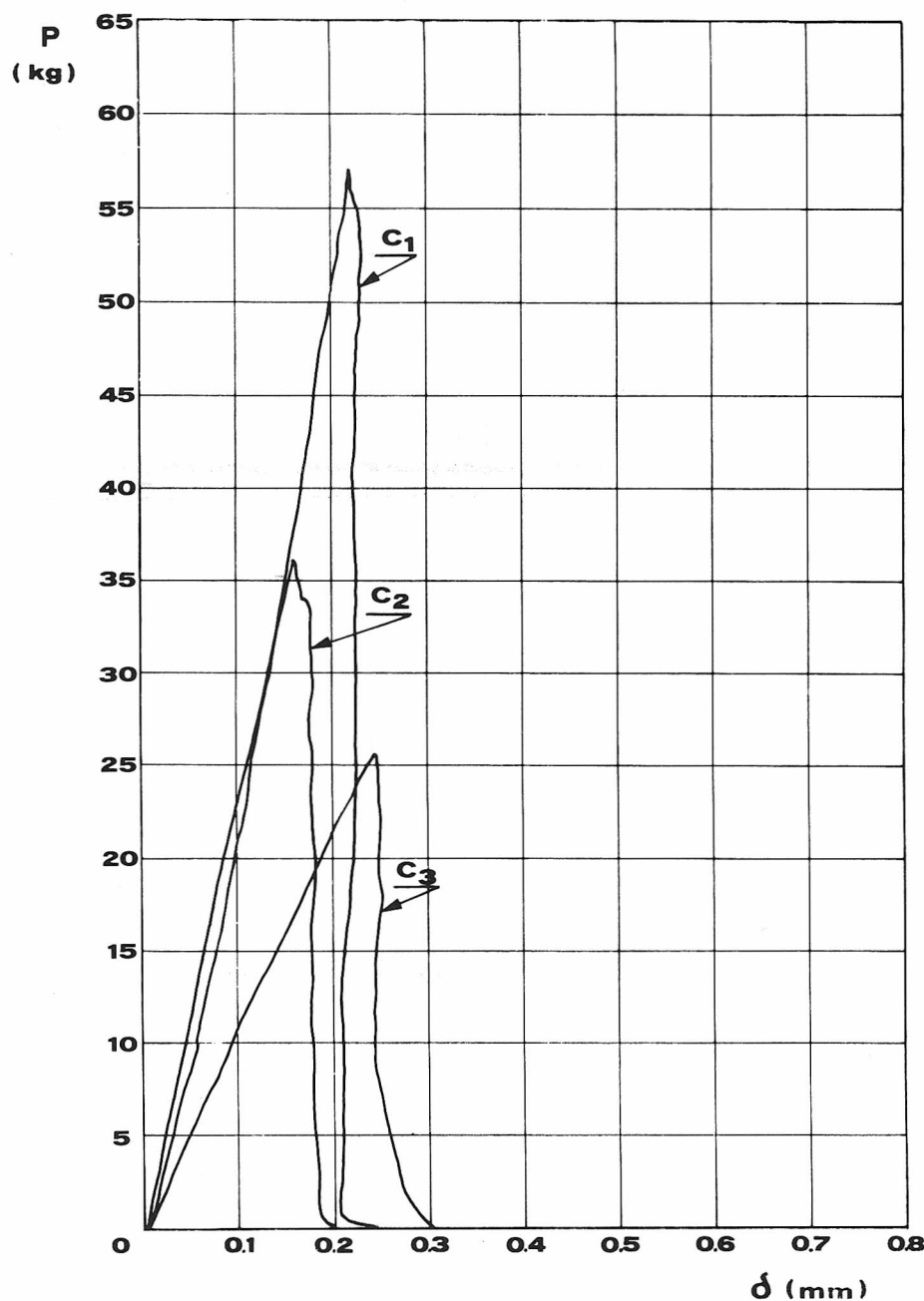


Fig. 10 Load-deflection diagrams obtained experimentally on masonry of the 20th century (material C).

sive crack model previously described, provides the load-deflection diagrams plotted in Fig. 11. Theoretical and experimental results present very similar softening branches. For the specimens with shallow initial notch (A1, B1, C1) a snap-back instability is predicted by the model. Such an instability is revealed by the experimental investigation. As a matter of fact, the softening branch presents a positive slope in these cases and, while load and deflection both decrease, in the meantime the crack mouth opening displacement (which is the controlling parameter) and crack length increase. A phenomenon which is catastrophic and unstable in na-

ture is made stable in practice by controlling a monotonically increasing function of time. It is therefore demonstrated that the cohesive crack model describes brick masonry failure as accurately as in the case of concrete.

The ratio of the experimental peak load to the maximum load derived from a linear elastic fracture mechanics (LEFM) analysis, $P_{\text{exp}}/P_{\text{LEFM}}$, is represented in Fig. 12 as a function of the relative crack depth a/H . Such a ratio is nearly constant for each material and always lower than unity. LEFM, i.e. the critical condition $K_I = K_{IC}$, is not a conservative criterion when the specimen sizes are comparatively small [9–12]. In addition to

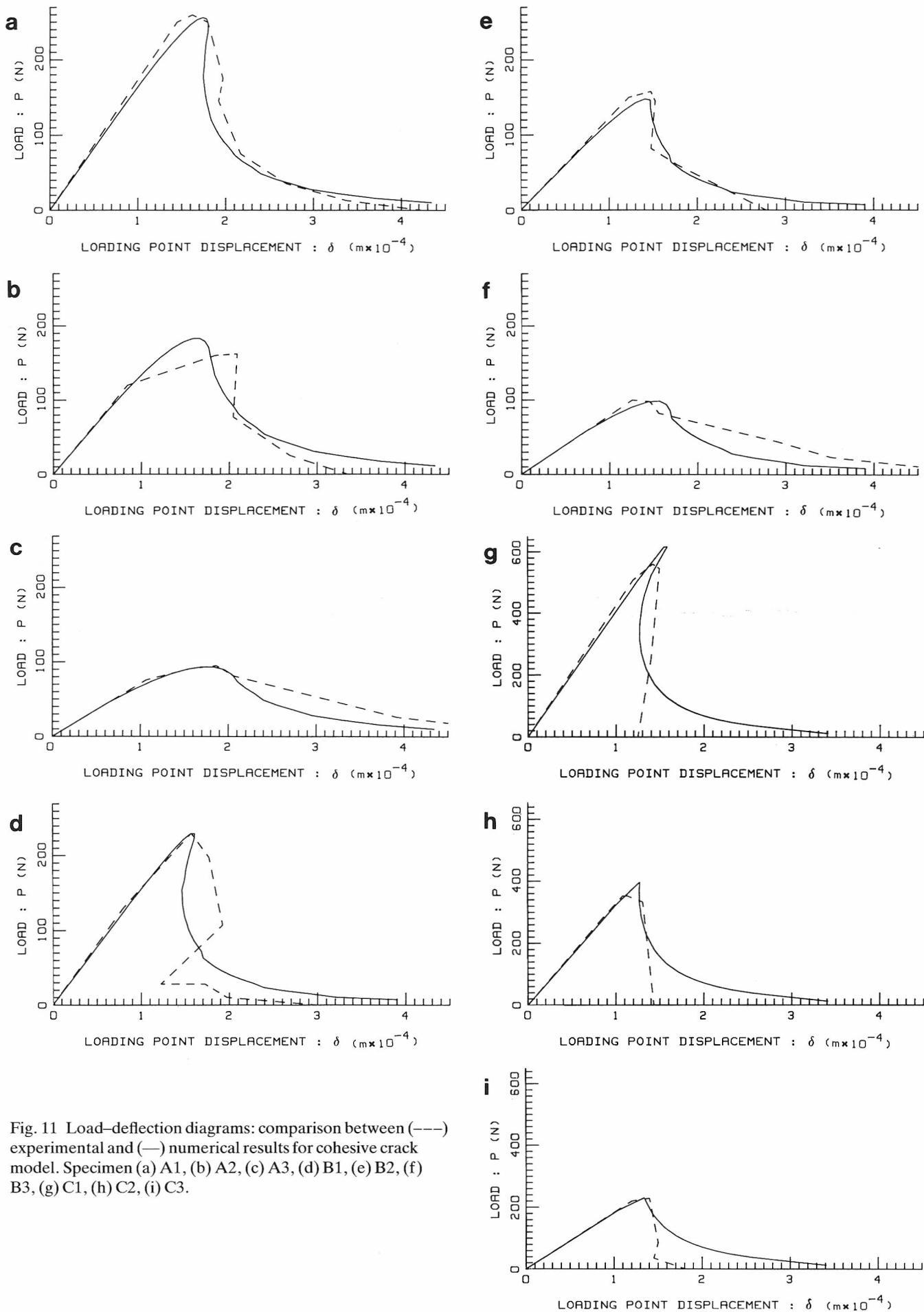


Fig. 11 Load-deflection diagrams: comparison between (---) experimental and (—) numerical results for cohesive crack model. Specimen (a) A1, (b) A2, (c) A3, (d) B1, (e) B2, (f) B3, (g) C1, (h) C2, (i) C3.

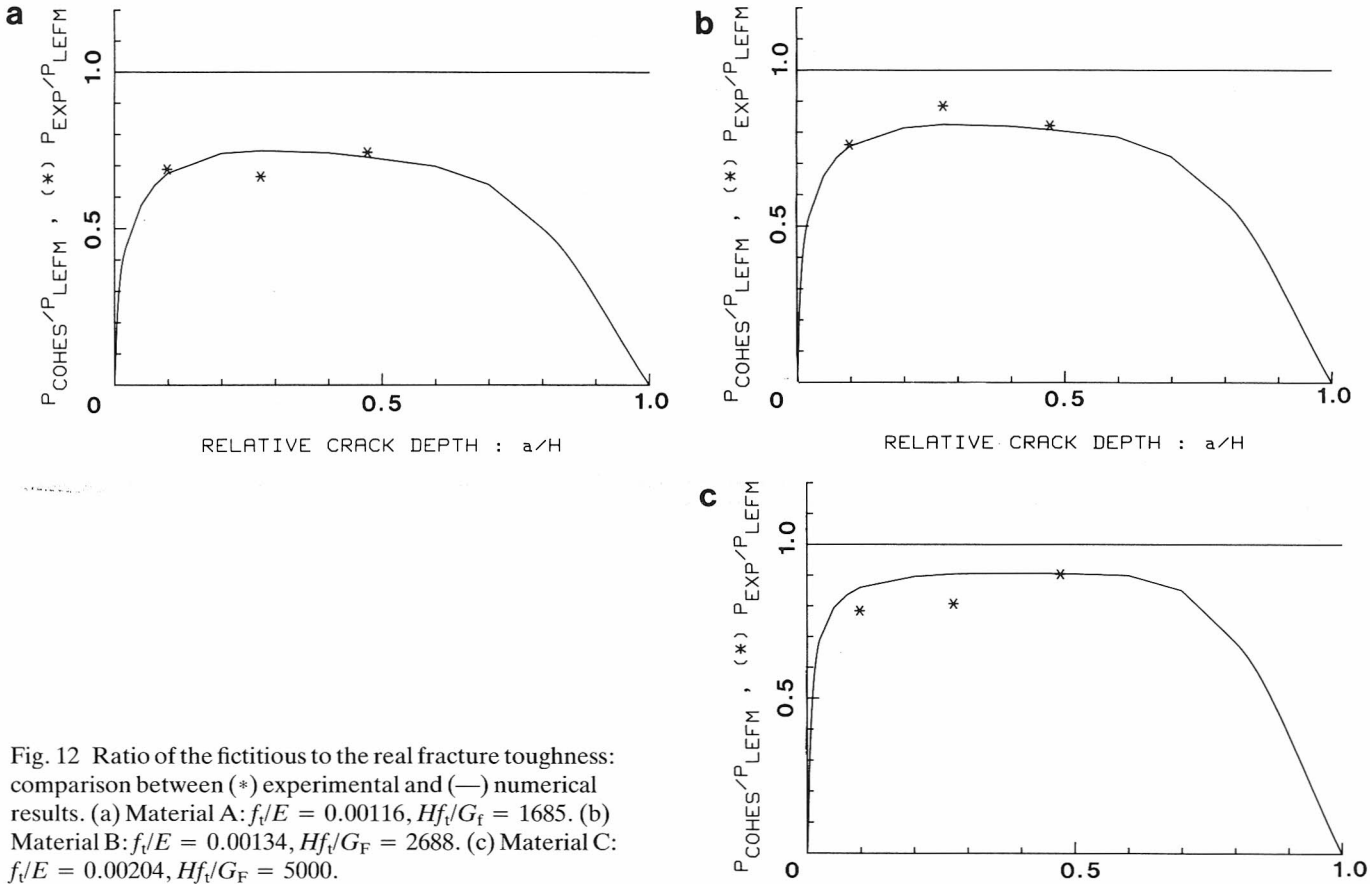


Fig. 12 Ratio of the fictitious to the real fracture toughness: comparison between (*) experimental and (—) numerical results. (a) Material A: $f_t/E = 0.00116$, $Hf_t/G_f = 1685$. (b) Material B: $f_t/E = 0.00134$, $Hf_t/G_f = 2688$. (c) Material C: $f_t/E = 0.00204$, $Hf_t/G_f = 5000$.

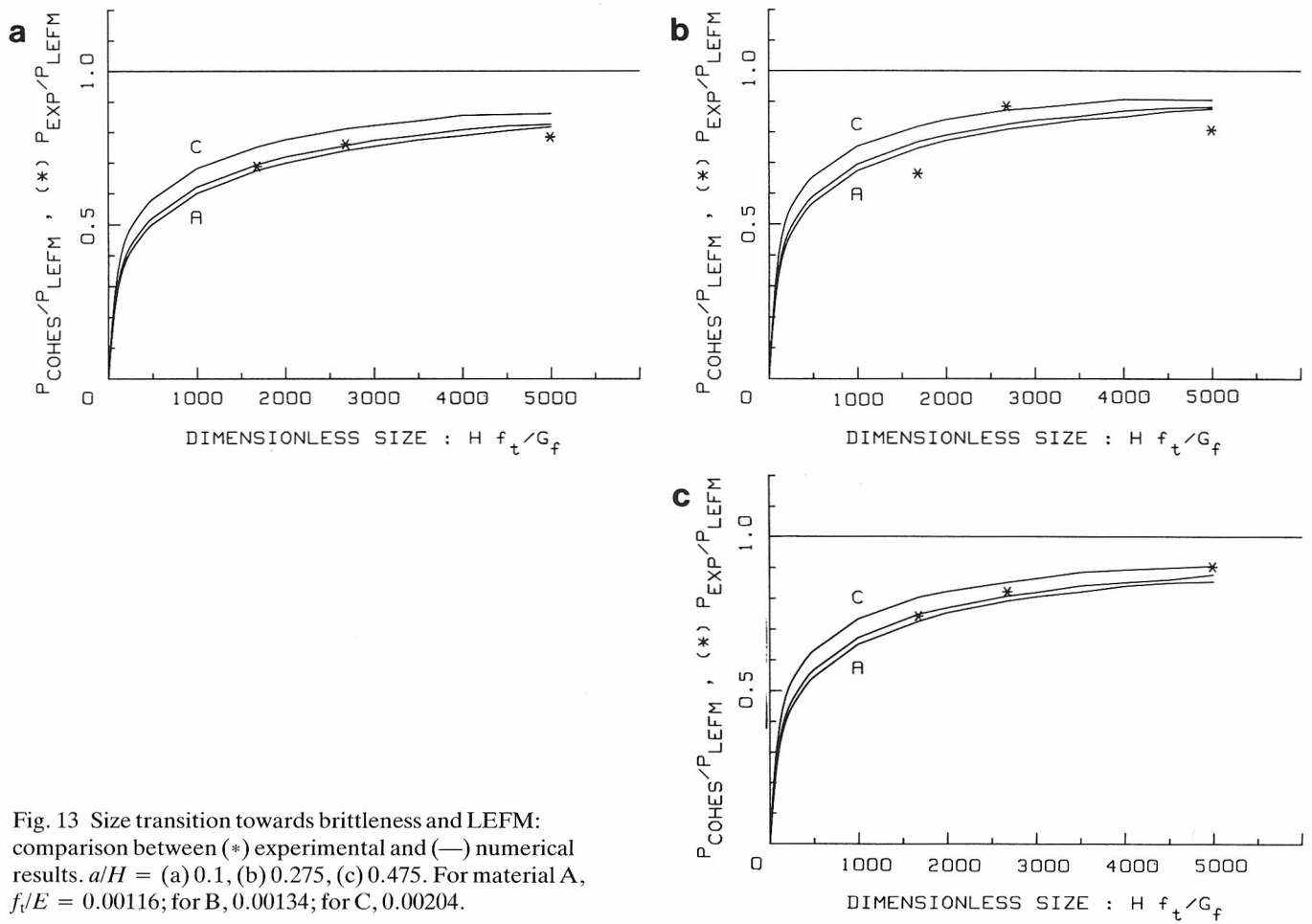


Fig. 13 Size transition towards brittleness and LEFM: comparison between (*) experimental and (—) numerical results. $a/H =$ (a) 0.1, (b) 0.275, (c) 0.475. For material A, $f_t/E = 0.00116$; for B, 0.00134; for C, 0.00204.

the experimental data, the ratio of the theoretical cohesive peak load to the maximum LEFM load, $P_{\text{cohes}}/P_{\text{LEFM}}$, is plotted in Fig. 12 as a function of the relative crack depth a/H . The theoretical curves approximate the experimental data very accurately. For initial notch depths lower or higher than those selected for the experimental investigation, a decrease of the ratio $P_{\text{exp}}/P_{\text{LEFM}}$ is expected. The theoretical curve $P_{\text{cohes}}/P_{\text{LEFM}}$ thus presents a bell-shape, achieving a maximum value for $a/H \approx 0.3$ and tending to zero for $a/H \rightarrow 0^+$ and $a/H \rightarrow 1^-$. Such a result may also be predicted by applying dimensional analysis and considering the competition between brittle fracture collapse due to stress-intensification and ultimate strength collapse at the ligament [9–12].

The two non-dimensional numbers $\varepsilon_t = f_t/E$ and $1/s_E = Hf_t/G_F$ are reported in the legend of Fig. 12. The ratio $P_{\text{exp}}/P_{\text{LEFM}}$ unequivocally increases by increasing such numbers. This is due to the high notch sensitivity and brittleness that the structural response shows for material C (Fig. 10). The peak load may be predicted by LEFM much more accurately for specimens C than for specimens A. On the other hand, the bell-shaped curves for material A would rise if larger specimens were utilized. The physical behaviour is in fact similar if the brittleness number Hf_t/G_F is the same. We can expect the behaviour of material A to be as brittle as that of material C when the size-scale of specimen A is about three times that of the present investigation, i.e. $H \approx 12$ cm.

The same ratios previously discussed, $P_{\text{exp}}/P_{\text{LEFM}}$ and $P_{\text{cohes}}/P_{\text{LEFM}}$, are reported in Fig. 13 as functions of the dimensionless size Hf_t/G_F . One numerical curve for each material, i.e. for each dimensionless number f_t/E , and for each crack depth a/H , is plotted in Fig. 13. The curves related to the same crack depth are very close, the maximum load provided by the cohesive crack model being not very sensitive to the ratio f_t/E . In each case selected for the investigation, an evident transition appears from an ultimate strength collapse at the ligament

$$\sigma_{\text{nom}} = \frac{Pl}{4} \frac{6}{b(H-a)^2} = f_t \quad (7)$$

to a brittle crack propagation due to stress-intensification

$$K_I = K_{IC} \quad (8)$$

REFERENCES

1. Page, A. W., 'An experimental investigation of the biaxial strength of brick masonry', in Proceedings of 6th I.B.M.A.C., Rome, May 1982, pp. 3–19.
2. Bocca, P. and Levi, F., 'Indagini sistematiche su muratura in blocchi di argilla espansa', *Quaderni Anpae* Nr. 3 (1983) 3–10.
3. Drysdale, R. G. and Hamid, A. A., 'Tension failure criteria for plain concrete masonry', *J. Struct. Engng ASCE* 110 (2) (1984) 228–244.
4. Carpinteri, A., 'Interpretation of the Griffith instability as a bifurcation of the global equilibrium', in Proceedings on 'Application of Fracture Mechanics to Cementitious Composites', NATO Advanced Research Workshop, September 1984, Northwestern University, edited by S. P. Shah (Nijhoff, 1985) pp. 287–316.
5. Hillerborg, A., Modeer, M. and Petersson, P. E., 'Analysis of crack formation and crack growth in concrete by means of fracture mechanics and finite elements', *Cem. Concr. Res.* (1976) 773–782.
6. Scott, M. W. and Abrams, D. P., 'Mechanics of masonry in compression', *J. Struct. Engng ASCE* 111 (4) (1985) 857–870.
7. Carpinteri, A., Marega, C. and Savadori, A., 'Size effects and ductile–brittle transition of polypropylene', *J. Mater. Sci.*, 21 (1986) 4173–4178.
8. RILEM Draft Recommendation 'Determination of the fracture energy of mortar and concrete by means of three-point bend tests on notched beams', *Mater. Struct.* 18 (106) (1985) 285–290.
9. Carpinteri, A., 'Static and energetic fracture parameters for rocks and concretes', *ibid.* 14 (1981) 151–162.
10. *Idem*, 'Notch sensitivity in fracture testing of aggregative materials', *Engng Fract. Mech.* 16 (1982) 467–481.
11. *Idem*, 'Application of fracture mechanics to concrete structures', *J. Struct. Div. ASCE* 108 (1982) 833–848.
12. Wecharatana, M. and Shah, S. P., 'Prediction of nonlinear fracture process zone in concrete', *J. Engng Mech. ASCE* 109 (1983) 1231–1246.